

Growth and simulation of high-aspect ratio nanopillars by primary and secondary electron-induced deposition

J. D. Fowlkes,^{a)} S. J. Randolph, and P. D. Rack
*The University of Tennessee, Knoxville, The Department of Materials Science and Engineering,
434 Dougherty Engineering Building, Knoxville, Tennessee 37996-2200*

(Received 2 June 2005; accepted 6 September 2005; published 2 December 2005)

While several studies have suggested that secondary electrons dominate electron beam induced deposition (EBID), we demonstrate that primary electrons (PE's) contribute significantly to the deposition for nanoscale EBID over the electron beam energy range (500–20 keV). High-aspect ratio pillar growth is a signature of EBID; W nanopillar growth on SiO₂ substrate yielded a growth rate of 6 nm s⁻¹ and a nanopillar aspect ratio of ~50. A simple integration of the primary, secondary, and backscattered electron distributions versus a dissociation cross section for WF₆ suggests that all three electron species should contribute to the total volume of the deposited nanopillar, contrary to reports that suggest that secondary electrons dominate the process. A three-dimensional, Monte Carlo simulation including time correlated gas dynamics and species specific deposition was developed to help elucidate which of the relevant electron species, primary (PE's), secondary (SE's), and/or backscattered electrons (BSE's), induce the dissociation of precursor gas and lead to nanopillar growth. PE's and secondary electrons produced from the incident beam (SE^I's) were found to induce the vertical nanopillar growth component relative to secondary electrons induced from backscattered electrons (SE^{II}'s) and BSE's. © 2005 American Vacuum Society.

[DOI: 10.1116/1.2101732]

I. INTRODUCTION

The controlled growth and manipulation of materials at the nanoscale is a crucial element for the future of nanotechnology. Specifically, the future of nanoscale processing and nanomanufacturing will require site-selective directed assembly techniques for critical level processing. Current techniques to selectively deposit or etch microscopic features utilize ion beam deposition and etching, laser ablative etching using far field and near field optics, and mechanical abrasion using a fine microtip. Of these techniques, focused ion beam (FIB) processing is probably the most mature technology that has been extended into the nanoscale.¹ While suitable for many applications, FIB processing has several drawbacks that make it difficult to extend to many nanoscale applications. The most severe drawback when using a gallium focused ion beam is the gallium implantation into the substrate, which can deleteriously change the physical properties (optical, electrical, mechanical, biological...) of the substrate.² Additionally, charging inherent to the ion-solid interaction causes proximity effects and can also lead to so-called "riverbed effects" which erodes nearby features when the heavy ion beam is scattered and induces sputtering. Consequently, while FIB processing is a very effective technique in many microscale applications,^{3–10} an alternative damage-free site-selective processing technique is needed for emerging nanoscale processing applications.

Focused electron beam processing or electron-beam induced deposition (EBID) has been demonstrated as a viable technique for depositing microscopic and nanoscopic mate-

rials. Broers *et al.*¹¹ were the first to make use of so-called contamination staining observed in electron microscopy to grow very thin metal lines by the electron stimulated decomposition of a metal containing precursor gas. Subsequent to this, a variety of materials have been deposited using a focused or a broad electron source including carbon,¹² copper,¹³ chromium,¹⁴ gold,^{15–18} iron,^{19,20} silicon,²¹ silicon oxide,²² palladium,²³ platinum,^{24,25} tungsten,^{26–35} and zirconium oxide.³⁶ For example, a feature size as small as 8.3 nm was deposited at high energies (200 keV) in a scanning transmission electron microscope.³⁷ Kohlmann-von Platen *et al.* deposited tungsten nanopillars by electron beam stimulated dissociation of W(CO)₆ precursor gas; secondary electrons were suggested to control nanopillar diameter over the entire growth cycle because the Gaussian tails of the incident beam slowly widen the growing nanopillar at the base due to secondary electron stimulated EBID.³⁸ Hiroshima and Komuro deposited W wires from the EBID of WF₆ precursor³⁹ by a beam raster process and also attributed nanopillar diameter growth to SE stimulated deposition. Koops *et al.* indicated that BSE's induced deposition at the flanks of growing features and limited the aspect ratio achievable by an electron-stimulated process.⁴⁰

II. EXPERIMENT

A. Experimental nanopillar growth

In this work, we have used a custom-built gas delivery system affixed to a Hitachi 4300-SN scanning electron microscope (SEM). The details of the gas delivery system are described in detail elsewhere.³⁵ Figure 1 illustrates a deposited tungsten nanopillar grown under the following condi-

^{a)}Author to whom correspondence should be addressed; electronic mail: fowlkesjd@ornl.gov

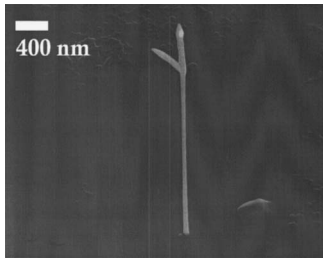


FIG. 1. W nanopillar deposited on SiO_2 substrate with a primary beam energy of $E_0=30$ keV and $i_B=50$ pA. The nanopillar was grown for $t=10$ min in 6.0×10^{-3} Torr WF_6 precursor. A Hitachi 4300 SEM was used with the microscope parameters of working distance (WD)=6.5 mm, in stationary spot mode at a magnification of $\times 30000$.

tions: spot or stationary beam mode, 30 keV beam energy, 50 pA beam current, 6.0×10^{-5} Torr WF_6 background pressure, an estimated flux enhancement factor of 100 [WF_6 gas flux of $\sim 7.0 \times 10^{15}$ $\text{WF}_6/(\text{cm}^2 \text{ s})$] on a SiO_2 thin film substrate. The nanopillar exhibited a very high aspect ratio due to the high vertical growth rate of the structure with a nearly cylindrical morphology. The aspect ratio for the tungsten nanopillar shown is ~ 50 where the final height of the nanopillar is $3.6 \mu\text{m}$ (6 nm s^{-1} growth rate) and the full width at half maximum (FWHM) of the nanopillar is 68 nm. The side branch protruding from the nanopillar template was grown by tilting the substrate illustrating the potential for three-dimensional processing.

B. Summary of three-dimensional Monte Carlo based EBID predictor

A three-dimensional, Monte Carlo simulation was developed to help elucidate which of the relevant electron species emitted from the surface during irradiation, among PE's, SE's, and BSE's, induce the dissociation of precursor gas and lead to nanopillar growth. The role of this article is not to provide the details of the simulation but rather to use the results of the simulation to aid in understanding the EBID process. The details of the model will be described in a subsequent publication. The probability of deposition by PE's, SE's, and BSE's as a function of primary beam energy, the growth rate of the nanopillar due to each species, and the role each plays in the development of the nanopillar morphology are simulated and discussed. In addition, a dissociation cross section for WF_6 gas is derived from the total ionization cross section of this molecule and justification is made for the derivation process. The probability of deposition per electron species is discussed. The model system used for the simulations was W deposited on an atomically flat germanium (Ge) substrate by the dissociation of WF_6 precursor gas. As a representative example it was found that at an electron accelerating voltage (E_0) of 5 keV, all electron species contributed significantly to the *volume* of the W deposit. However, the PE's and SE^I's interact with the nanopillar over a much narrower spatial extent than do the SE^{II}'s and BSE's and hence exhibited a higher *current density* over the nanopillar surface. As a result, the PE's and SE^I's were found to induce

the *vertical growth* and the BSE's and SE^{II}'s contribute to radial broadening of the nanopillars.

III. APPROXIMATE WF_6 DISSOCIATION CROSS SECTION

A significant drawback to the development of an accurate EBID simulator is the deficiency of dissociation cross-section data for precursor gas species. This is due primarily to the difficulties associated with performing experiments of this type; the detection of neutral products following dissociation events is difficult. The available data from literature sources applies predominantly to simple gases such as H_2 and N_2 ⁴¹ and carbon based species such as CH_y .⁴² Experiments to determine the ionization cross section are far easier to perform. Here, the total ionization cross section for WF_6 gas was slightly modified to better represent a dissociation cross section and used in our EBID simulation. It is well documented that the *shape* of the ionization and dissociation cross-section curves are similar.^{43,44} For most molecules the dissociation cross section has a *lower threshold energy*, a *maximum at lower electron energies*, and also has a *higher maximum value* than the ionization cross section. Consequently, the total ionization cross section was modified by: (1) shifting the threshold ionization energy to a lower value of $E=5.7$ eV which is the W-F bond energy and, (2) by scaling the value of the cross section at low energies $12 \text{ eV} \leq E \leq 100 \text{ eV}$ where dissociation events are more probable than ionization events relative to C_2H_5 for which both dissociation and ionization data are available. The EBID of C_2H_5 was simulated first by Silvis-Cividjian *et al.*³⁷ based on the data of Alman Ruzic, and Brooks.⁴³ The same data have been used in this work for two reasons: to correct the WF_6 ionization cross section in order to make it resemble more a dissociation cross section and to have a benchmark for comparing our simulation with that of Silvis-Cividjian.³⁷

The total ionization cross section for electron scattering from WF_6 as a function of energy $\sigma(E)$ was determined by Basner, Schmidt, and Deutsch experimentally and reprinted by Kwitniewski, Ptasinska-Denga, and Szmytkowski.^{45,46} Our approach is to reproduce the data from Kwitniewski and co-workers in a functional form commonly used for ionization cross sections⁴⁷⁻⁴⁹ using a fitting algorithm in the MATHEMATICA® software package. The algorithm yielded an equation of the form

$$\sigma(E) = \left(A_1 \left(1 - \frac{1}{E} \right) + A_2 \left(1 - \frac{1}{E} \right)^2 + A_3 \left(\frac{\log E}{E} \right) + A_4 \log E \right) \frac{1}{E}, \quad (1)$$

where the A_x 's represent constants and E is the electron energy.^{47,48} MATHEMATICA® applies a least-squares fit to a linear combination of input functions and approximates the data. This equation was derived from the binary-encounter-Bethe model⁴⁹ which combines the Mott cross section and the high temperature behavior of the Bethe cross section. This functional form is typically reported for energies up to

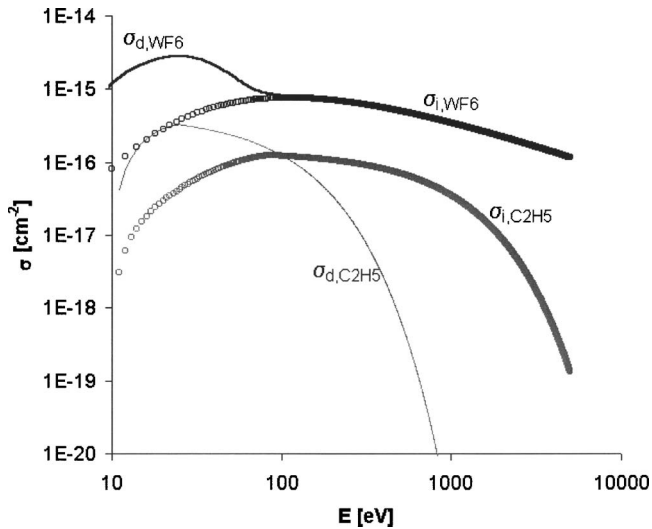


FIG. 2. Approximate dissociation cross section for WF_6 gas ($\log \sigma$ vs $\log E$) estimated from the experimental determined ionization cross section for WF_6 (see Refs. 45 and 46) and the estimated dissociation and ionization cross sections for C_2H_5 based on extrapolations from experimental data on CH_x species (see Ref. 43).

5 keV, but is expected to be a reasonable approximation for the energies reported here as the drop off in σ with increasing energy is much less severe than reported in Ref. 43.

The total ionization cross section was subsequently modified to approximate the dissociation cross section for WF_6 . Silvis-Cividjian⁵⁰ simulated the deposition of carbon at high beam energies ($E_0 > 20$ keV) using the estimated dissociation cross section for C_2H_5 from Alman, Rugic, and Brooke.⁴³ We applied a scaling procedure based on the ratio of dissociation cross section for C_2H_5 ($\sigma_{d,\text{C}_2\text{H}_5}$) and the ionization cross section for C_2H_5 ($\sigma_{i,\text{C}_2\text{H}_5}$)

$$\sigma_{d,\text{WF}_6} = \left[\frac{\sigma_{d,\text{C}_2\text{H}_5}}{\sigma_{i,\text{C}_2\text{H}_5}} \right] \cdot \sigma_{i,\text{WF}_6}, \quad \text{for } \frac{\sigma_{d,\text{C}_2\text{H}_5}}{\sigma_{i,\text{C}_2\text{H}_5}} \geq 1, \quad (2)$$

$$\sigma_{d,\text{WF}_6} = \sigma_{i,\text{WF}_6}, \quad \text{for } \frac{\sigma_{d,\text{C}_2\text{H}_5}}{\sigma_{i,\text{C}_2\text{H}_5}} < 1. \quad (3)$$

Molecular dissociation occurs preferentially at low energies ($E < 100$ eV) relative to ionization for most molecules and Eq. (2) modifies the ionization cross section to account for this. Figure 2 shows a plot of the ionization total cross section for WF_6 shown superimposed with the modified dissociation cross section, and the dissociation and ionization cross section for C_2H_5 from Alman, Rugic, and Brooke⁴³ and used by Silvis-Cividjian *et al.*³⁷ For electron energies $E > 100$ eV the modified dissociation cross section and ionization total cross section were assumed to be equivalent. This was done based on the fact that the dissociation cross section in Ref. 43 for C_2H_5 decreases in magnitude too steeply beyond 25 eV. For example, the dissociation cross section decreases ten orders of magnitude from $E = 120$ eV to $E = 1900$ eV based on the functionality applied by Alman, Rugic, and Brooke.⁴³ This is a severe underesti-

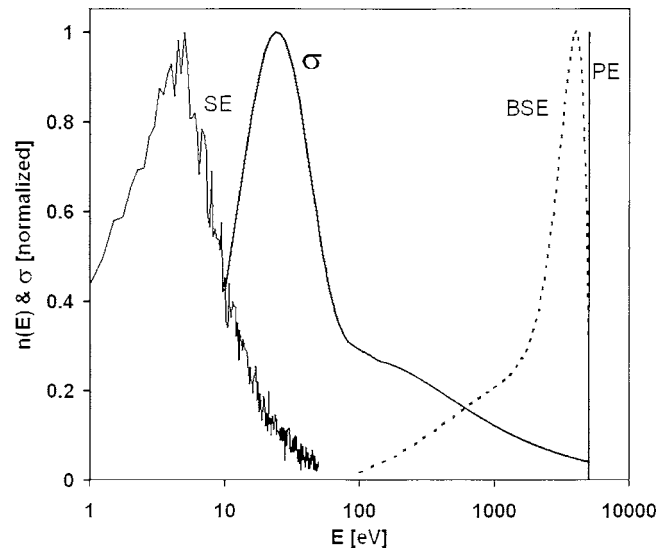


FIG. 3. Secondary (SE) and backscattered (BSE) energy distributions from a flat Ge substrate derived by a Monte Carlo simulation of 5000 electrons (an average of ten simulations) superimposed with the approximated WF_6 dissociation cross section. All distributions and cross sections have been normalized to unity and the energy axis is plotted in logarithmic form.

mation of the dissociation probability at high energy and is related to the fitting procedure used⁴³ as they were interested primarily in the accuracy of fit at low energies. In the case of CF_4 , the measured dissociation cross section at $E = 600$ eV is only one half of the value of the maximum at $E = 100$ eV,⁵¹ which illustrates that there is less severe drop in dissociation cross section with energy relative to what is used in Ref. 37. The curve fitting described in Ref. 43 applied to CH_3 and CH_2 data⁴² was fit for the energy range of 0–100 eV, which makes it impractical for use at high energies. Moreover, Alman and co-workers extrapolated the cross sections for C_xH_y species from CH_y data due to the difficulties associated with collecting dissociation cross section experimental data for heavier hydrocarbon species. Hence, we feel that the probability of dissociation at high energies is strongly underestimated by extrapolating the data from Alman⁴³ and we assume that the total ionization cross section is a reasonable approximation of the dissociation cross section at $E > 100$ eV. We also speculate that ionization events could also induce deposition via exchange processes, because when the SE yield is < 1 the near surface region should be negatively charged.

Figure 3 shows the approximated dissociation cross section up to an electron energy of 5 keV. Also shown in Fig. 3 is a representative and normalized secondary electron (SE) and BSE distribution for germanium at 5 keV that were generated by a Monte Carlo scattering based simulation. Monte Carlo simulations of electron-solid interactions have been shown to accurately and precisely predict the spatial distribution of SE and BSE species as well as the energy distribution of BSE species.^{52,53} Simple empirical models that incorporate experimental results to “calibrate” SE emission have also accurately predicted the energy profiles of emitted SE’s.^{54,55}

TABLE I. Calculated (n_d) and simulated (n_{dm}) number of dissociation events per 5000 virtual electrons. Each dissociation event induces the deposition of one W atom. The complete table consists of the ($r_{\text{interaction}}$) average radius of the interaction area for each species, coefficients, current, current density, probability of dissociation (Q), and the probability of dissociation normalized to the interaction area and the probability of dissociation by primary electrons (Q_{area}). The white column for $n_{d,m}$ represents the simulated number of dissociation events per species if that species were only one capable of dissociation. The gray column for $n_{d,md}$ represents the simulated number of dissociation events for coupled interactions between electron species.

	$f_{\text{interaction}}$ [nm]	Coefficient $\eta, \delta_1, \& \delta_2$	I [pA]	$I_{d,\text{avg.}}$ [pA/nm ²]	Q	n_d for 5000 e ⁻	n_{dm} for 5000 e ⁻	n_{dmd} for 5000 e ⁻	Q_{area} normalized
PE	2.5	1	0.615	3.13E-02	0.183	915	901	901	1.00
SE ^I	2.5	0.436	0.268	1.37E-02	0.155	775	783	658	0.85
SE ^{II}	5.6	0.809	0.165	1.68E-03	0.100	500	443	430	1.09E-01
BSE	120	0.332	0.204	4.51E-06	0.019	95	97	93	4.51E-05

IV. CALCULATED AND SIMULATED NANOPILLAR GROWTH BY EBID

A. Dissociation probability

The probability Q of electron-induced molecular dissociation per electron is governed by the following analytical expression that represents a macroscopic dissociation probability:

$$Q = \frac{\theta \cdot S_p}{n_{PE}} \cdot \int_{E_i}^{E_f} n_x(x, y, t, E) \cdot \sigma(E) dE, \quad (4)$$

where $n_x(E)$ is the electron energy distribution (Fig. 3) of the particular electron species and where $x=SE_I, SE_{II}, BSE,$ or $PE, \sigma(E)$ is the dissociation cross section and θ is the percentage surface coverage of adsorbed precursor molecules and S_p is the atomic surface site density. In the case of all types of electron species, the electron energy distributions are a function of nanopillar shape and size which continuously changes during growth. Equation (4) was used to calculate the probability of dissociation of WF_6 by PE, BSE, SE^I , and SE^{II} species on a Ge substrate and the growing tungsten nanopillar to determine which electron species induces the most dissociation events per incident electron. The number of electrons versus energy $n(E)$ was generated using a Monte Carlo simulation to generate probable electron trajectories in an atomically flat Ge substrate at 5 keV. The normalized $n(E)$ spectra for BSE and SE's is shown in Fig. 3 superimposed with the approximated WF_6 dissociation cross section. The output BSE (η) and SE (δ) coefficients from the simulation closely match experimental values of δ and η for Ge irradiated at $E_0=5$ keV; namely $\delta=0.704$ and $\eta=0.332$. These coefficients are not expressed explicitly in Eq. (4) but rather are accounted for in the Monte Carlo simulation, specifically in the term $n(E)$. For example, for the case of backscattered electrons, the coefficient is implicitly contained in Eq. (4) in the integral term as

$$\int_{50 \text{ eV}_i}^{E_0} n_{BSE}(E) dE = \eta I_b, \quad (5)$$

where ηI_b is the area underneath the backscattered electron energy distribution.

Initially it was expected that SE-induced deposition would be the sole or dominant contributor to nanopillar growth based on existing works in experimental and simu-

lated EBID.^{32,37-39} However, our initial calculations indicated that PEs are a significant EBID growth source. Table I lists the dissociation probability Q for PE, SE^I , SE^{II} , and BSE's obtained by evaluating the integral in Eq. (4) using Simpson's approximation and the energy distributions from Fig. 3 for $E_0=5$ keV and 5 nm FWHM Gaussian beam irradiation of a flat, Ge substrate surface covered with WF_6 precursor ($\theta=1$) and an SE_I, SE_{II} and BSE coefficient of $\delta_1=0.436, \delta_2=0.809,$ and $\eta=0.332,$ respectively. The simulation was run to validate the analytical calculations of the contribution of the different electron species to EBID growth. The simulation conditions began with a surface coverage of $\theta=1$ (assuming Langmuir adsorption) and EBID was allowed to propagate with $P_{WF_6}=80$ Torr and an average desorption time $\tau=\infty$. While this localized pressure is relatively high compared to normal EBID experimental conditions, this pressure is required to illustrate the case of a saturated surface ($\theta=1$) at all times. Thus, this represents a case in which the process is reaction rate limited. In future publications, we will elaborate on the effect of mass transport limited processes. The simulator updates the surface coverage per incident electron. Figure 4 shows a macroscopic illustration of a W nanopillar that has grown to a noticeable height above the Ge substrate surface. The electron trajectory shown in the diagram was chosen to illustrate

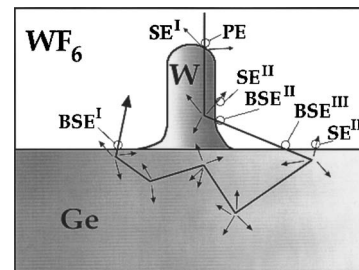


FIG. 4. Illustrated cross section through the central axis of a deposited W nanopillar and a possible electron trajectory through the WF_6 -Ge-W material set. Six deposition events are possible and are indicated in the figure. Backscattered electrons (BSE's) may induce deposition on leaving the nanopillar surface (BSE^I), on reentry into the Ge substrate (BSE^{III}), and/or on exiting the Ge surface (BSE^I). Secondary electrons have a very shallow escape depth and may induce deposition, following their creation just below the surface, when a primary electron enters the surface, within $\sim 5\lambda$ of the electron entry point (SE^I), or following their creation when a backscattered electron leaves the surface (SE^{II}).

TABLE II. Simulated, average secondary electron coefficient (δ for the W nanopillar) as a function of incident electron beam energy, and the standard deviation. The magnitude of SE-induced deposition scales with the secondary electron coefficient (see Fig. 5).

E_0 [eV]	δ	$\pm\Delta\delta$
500	1.243	0.01
2000	1.404	0.011
5000	0.735	0.005
10 000	0.424	0.007

all of the possible types of dissociation and deposition events. The total contribution from the three possible BSE deposition events labeled in Fig. 4 has been collapsed into one term and referred to BSE throughout this article due to the minimal contribution of BSE's to the total growth process. Table I shows that the probability for deposition is highest for EBID by PE's ($Q=0.183$) and SE^I's ($Q=0.155$) while SE^{II}'s ($Q=0.100$) and BSE's ($Q=0.019$) are slightly less probable. The number of species dissociated per electron (n_d) was then calculated simply as $n_d = n_e \times Q$ where n_e is the number of electrons and in the case for Table I was set to 5000. The adjacent column labeled n_{dm} represents the number of species dissociated per electron type *as simulated* by the three-dimensional Monte Carlo EBID simulation. For each type of electron, the dissociation probability was set to zero for the other electron species because in the simulation the dissociation probabilities are coupled via surface coverage. Thus, in order to compare these values with those calculated by Simpson's approximation (column n_d) the dissociation probabilities had to be decoupled. The coupling occurs as follows, if a PE enters the substrate and induces a deposition at a specific pixel (x, y), a SE^I generated by that PE may emerge from the surface through the same pixel (x, y). However, the gas previously adsorbed at that pixel could have been converted to tungsten by the PE-induced event. Thus, there is a dynamic component to the model where electron species have access to adsorbed gas in the following order: PE's have first access followed by SE^I's followed by SE^{II}'s and BSE's. This dynamic effect arises as a result of the frequency with which the surface coverage is updated in time. The surface coverage is updated after each primary electron either comes to rest in the solid or if it is backscattered and exits the surface in a positive (or upward) z direction. Moreover, this coupling simulates accurately the real situation considering the gas impingement is relatively slow relative to the production of secondary and backscattered electrons. The results of the dynamic, time-dependent simulation are listed in the gray shadowed column labeled as n_{dm} . The column reflects the initial access of PE's to the adsorbed surface layer; the number of atoms deposited per primary electron has not changed significantly between the decoupled and coupled simulations. However, the SE's are effected by the PE's having first access to the gas and the number of atoms deposited by SE^I's and SE^{II}'s was reduced 6.7%. The BSE's, on the other hand, have final access to the adsorbed layer yet the number of atoms deposited by this

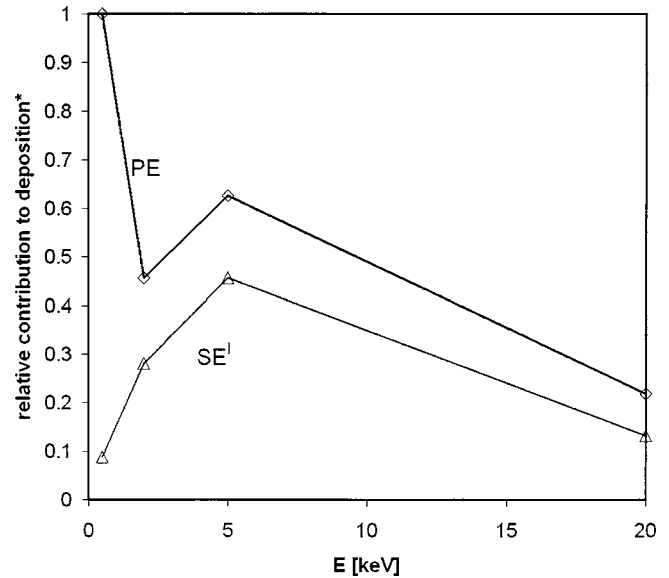


FIG. 5. Percent relative contribution to vertical nanopillar growth for PE and SE^I electron species. The simulation was carried out at $E_0=500, 2000, 5000,$ and $20\,000$ eV. The plot has been normalized to the percent relative contribution of PE's to the vertical growth rate at $E_0=500$ eV.

species does not change between the two simulations. The BSE's are emitted, however, from a significantly larger surface area $A = \pi \times 120 \text{ nm}^2$ (Table II) compared with the other electron species and hence have access to adsorbed gas around the perimeter of the main deposit where the other electrons species are not emitted.

The data in Table I, column Q represents the total probability of dissociation and deposition per electron species. This dissociation probability Q can be rearranged mathematically to represent the contribution of the electron species to the vertical growth velocity of the nanopillar (Q_{area}). Q_{area} is the probability a monolayer of atoms will be deposited normal to the substrate surface per electron species. The *area* subscript indicates that the probability has been normalized to the probability of deposition of a monolayer of atoms by PE's. The contribution of both SE^{II}- and BSE-induced deposition are strongly dependent on whether bulk, volumetric deposition (Q) or vertical, linear deposition (Q_{area}) is being considered. SE^{II}'s are one order of magnitude and BSE's are five orders of magnitude less likely to induce vertical nanopillar growth, respectively, than PE's based on the FWHM of their emission profiles from the surface. The effective current density of SE^{II}'s and BSE's emerging from the substrate is much lower than for the case of PE's and SE^I's because they emerge over a much larger area of surface as the nanopillar grows and hence the monolayer deposition rate for these species is significantly lower.

B. Vertical nanopillar growth by primary and secondary electrons

Figure 5 shows a plot of the simulated contribution of PE's and SE^I's to the vertical growth rate of a tungsten nanopillar versus electron beam accelerating voltage, from

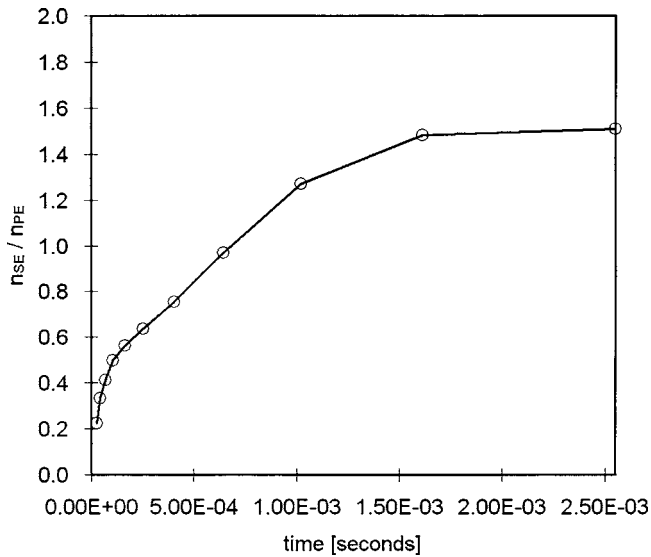


FIG. 6. Simulated ratio of the total number of W atoms deposited by secondary electrons (n_{SE}), SE^{I^1} 's + SE^{II^1} 's to the total number of W atoms deposited by primary electrons (n_{PE}). The contribution of secondary electrons to W deposition increases in time due to the evolution of the nanopillar structure.

$E_0=500$ eV to 20 keV, where the y axis is in the form of the percentage of monolayers deposited per electron species. SE^{II^1} 's and BSE's have not been included in the figure because they contribute insignificantly to the vertical growth rate of nanopillars as described in the previous paragraph. The simulations were carried out under the conditions of a saturated, monolayer surface coverage ($\theta=1$) using a beam current of $i_B=0.615$ pA. For this case, the growth rate is limited by the electron beam reaction with the precursor and not dependent on the precursor flux to the growth surface. PE's most significantly contributed to the final nanopillar height for all electron beam energies simulated while SE's contributed appreciably at the intermediate energies of 2 and 5 keV. The contribution to vertical growth by PE's steadily increased as the incident electron beam energy decreased. This trend is due entirely to the increased probability of precursor dissociation by PE's at low energy. The $n_{PE} \times \sigma(E)$ product steadily increases as the beam energy is decreased to $E_0=25$ eV and hence the probability of precursor dissociation is increased at lower beam energies. As opposed to PE-induced dissociation, secondary electron-induced deposition exhibited a maximum over the energy range studied. SE-induced deposition was found to correlate strongly with the number of SE's emitted from the W nanopillar per incident beam energy. The number of secondary electrons leaving the sample is expressed in terms of the primary incident beam current; for an incident current of i_B C/s, δi_b C/s of secondary electrons are emitted from the irradiated surface where δ is the secondary electron coefficient. Listed in Table II are the simulated secondary electron coefficients for each electron beam energy node. These simulated coefficients agree well with experimental values as the simulation was calibrated with experimental data for all beam energies. For example, Reimer and Tolkamp showed that at $E_0=1$ keV the second-

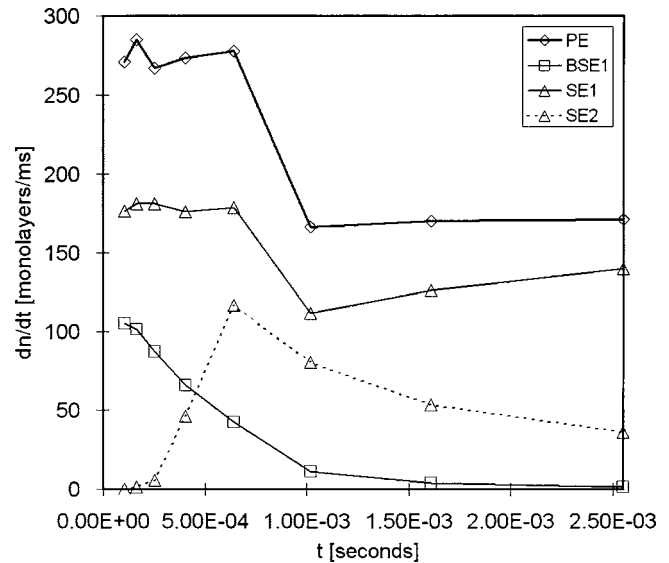


FIG. 7. Growth rates in monolayers tungsten/s separated based upon the electron species responsible for deposition. The PE's and SE^{I^1} 's most significantly contribute to the vertical growth of the W nanopillar.

ary electron coefficient was $\delta=1.64$, whereas at a higher beam energy of $E_0=10$ keV the coefficient dropped to $\delta=0.393$.⁵⁶ The dissociation induced by SE's was a maximum at $E_0=2$ keV (Fig. 4) and corresponds to the energy at which the secondary electron coefficient for tungsten was a maximum ($\delta=1.404$, $E_0=2$ keV) for the four energies simulated (Table II).

Figure 6 shows a plot of the ratio of the total number of W atoms deposited by secondary electrons (n_{SE}), both SE^{I^1} 's and SE^{II^1} 's, to the total number of W atoms deposited by primary electrons (n_{PE}). Clearly, secondary electrons contribute more to the *volume* of W atoms in the growing aggregate as the simulation times increase and the nanopillar structure evolves. The number of secondary electrons escaping the W aggregate increases continuously up to $t < 1.5 \times 10^{-3}$ s due to the additional surface area evolving on the growing, vertical nanopillar structure ($h=4.5$ nm, FWHM=4.5 nm). The evolution of a nanopillar morphology leads to the emission of more secondary electrons because only secondary electrons generated near the surface have a likely probability of escape because of their short mean free path ($\lambda \sim 3-5$ nm). Hence, as the nanopillar aggregate develops a high-aspect ratio shape, more secondary electrons escape and the quantity of SE-induced dissociation increases.

Figure 7 is a plot of the nanopillar growth rate as a function of time for each contributing electron species. The data were derived from the same simulation as was used to produce Fig. 6. The *vertical* nanopillar growth rate in monolayers per second is highest for *primary* electrons. SE^{II^1} 's contribute less to vertical growth because these species induce deposition over the entire nanopillar *surface* while PE's induce deposition in the confined region of the Gaussian shaped beam. The growth rate curves for PE's and SE^{I^1} 's have the same shape because SE^{I^1} 's are generated by PE's as they enter the nanopillar aggregate and hence their mutual depen-

dence on morphology should be the same. However, as the nanopillar aggregate grows vertically, the surface area over which SE^{II} 's may induce deposition increases and hence more atoms are required to deposit a monolayer of W atoms as a function of time for SE^{II} 's. This effect is counterbalanced by the fact that more SE^{II} 's are emitted from the nanopillar structure but the deposition rate is still insufficient to rival the more significant mechanisms of PE and SE^I -induced growth. The simulation was terminated at steady-state nanopillar growth and this termination point was $t=2.5 \times 10^{-3}$ s. Beyond this time the electron interaction volume was confined to the nanopillar structure, with minimal penetration into the substrate, and PE, SE, and BSE growth rates reached steady state.

V. FUTURE OUTLOOK

This article represents our first description of the EBID simulator and compares the growth mechanisms for a reaction rate limited simulation. In future reports, we will show the utility of the simulation to predict: (1) morphology differences (cylindrical versus conical growth) as a function of the growth parameters; (2) lateral resolution versus nanostructure height for reaction and mass transport limited processes; (3) the effects that the deposited material (SiO_2 vs W) has on the morphology and resolution; (4) the effects that gas surface diffusion can have on the resolution and growth rate for an otherwise mass transport limited process.

VI. CONCLUSIONS

In summary, the simulation results of the EBID of W from WF_6 precursor on a Ge substrate for a host of beam energies revealed that high-aspect ratio growth dominates over the entire energy domain. The $E_0=5$ keV beam energy was studied by calculating and simulating the probability of EBID for PE's, SE^I 's, SE^{II} 's, and BSE's. The integration of the dissociation cross section \times electron species energy distribution product reveals that the PE's and SE^I 's should be the dominant species responsible for observed vertical W nanopillar growth. A Monte Carlo growth simulation was used to determine the energy and spatial distribution of each type of electron and was used to compare the probability that each electron has to dissociate the WF_6 precursor. The role that PE, SE, and BSE plays in the deposition process was determined in terms of how each species affects the vertical growth rate and resolution of nanopillar growth. PE's and SE^I 's induce vertical nanopillar growth because they are the most probable electron species to induce precursor dissociation and the subsequent deposition *and* their current densities are higher relative to SE^{II} 's and BSE's. The contribution of SE^I -EBID to nanopillar vertical growth velocity as a function of primary electron energy was found to correlate with the secondary electron coefficient.

ACKNOWLEDGMENT

This work was funded by DARPA-MTO Advanced Lithography Program.

- ¹T. Liang, A. Stivers, R. Livengood, P. Y. Yan, G. Zhang, and F. C. Lo, *J. Vac. Sci. Technol. B* **18**, 3216 (2000).
- ²T. Liang and A. Stivers, *Proc. SPIE* **4688**, 375 (2002).
- ³S. Matsui and Y. Ochiai, *Nanotechnology* **7**, 247 (1996).
- ⁴J. Melngailis, *Proc. SPIE* **1465**, 36 (1991).
- ⁵J. S. Ro, C. V. Thompson, and J. Melngailis, *J. Vac. Sci. Technol. B* **12**, 73 (1994).
- ⁶T. Tao, W. Wilkinson, and J. Melngailis, *J. Vac. Sci. Technol. B* **9**, 162 (1991).
- ⁷A. D. Dubner, A. Wagner, J. Melngailis, and C. V. Thompson, *J. Appl. Phys.* **70**, 665 (1991).
- ⁸J. C. Gonzalez, D. P. Griffis, T. T. Miao, and P. E. Russell, *J. Vac. Sci. Technol. B* **19**, 2539 (2001).
- ⁹K. Gamo, D. Takehara, Y. Hamamura, M. Tomita, and S. Namba, *Microelectron. Eng.* **5**, 163 (1986).
- ¹⁰Y. Fu, N. Kok, A. Bryan, and O. N. Shing, *Sens. Actuators, A* **88**, 58 (2001).
- ¹¹A. N. Broers, W. W. Molzen, J. J. Cuomo, and N. D. Wittels, *Appl. Phys. Lett.* **29**, 596 (1976).
- ¹²Y. Darici, P. H. Holloway, J. Sebastian, T. Trottier, S. Jones, and J. Rodriguez, *J. Vac. Sci. Technol. A* **17**, 692 (1999).
- ¹³M.-Y. Yen, C.-W. Chiu, F.-R. Chen, J.-J. Kai, C.-Y. Lee, and H.-T. Chiu, *Langmuir* **20**, 279 (2004).
- ¹⁴R. R. Kunz and T. M. Mayer, *J. Vac. Sci. Technol. B* **6**, 1557 (1988).
- ¹⁵K. L. Lee and M. Hatzakis, *J. Vac. Sci. Technol. A* **7**, 1941 (1989).
- ¹⁶I. Utke, P. Hoffmann, B. Dwir, K. Leifer, E. Kapon, and P. Doppelt, *J. Vac. Sci. Technol. B* **18**, 3168 (2000).
- ¹⁷A. Folch, J. Tejada, C. H. Peters, and M. S. Wrighton, *Appl. Phys. Lett.* **66**, 2080 (1995).
- ¹⁸K. Molhave, D. N. Madsen, A. M. Rasmussen, A. Carlsson, C. C. Appel, M. Brorson, C. J. H. Jacobsen, and P. Boggild, *Nano Lett.* **3**, 1499 (2003).
- ¹⁹R. R. Kunz, T. E. Allen, and T. M. Mayer, *J. Vac. Sci. Technol. B* **5**, 1427 (1987).
- ²⁰R. R. Kunz and T. M. Mayer, *Appl. Phys. Lett.* **50**, 962 (1987).
- ²¹S. Matsui and M. Mito, *Appl. Phys. Lett.* **53**, 1492 (1988).
- ²²S. Lipp, L. Frey, C. Lehrer, B. Frank, E. Demm, S. Pauthner, and H. Ryssel, *J. Vac. Sci. Technol. B* **14**, 3920 (1996).
- ²³T. J. Stark, T. M. Mayer, D. P. Griffis, and P. E. Russell, *J. Vac. Sci. Technol. B* **10**, 2685 (1992).
- ²⁴O. Yavas, C. Ochiai, M. Takai, A. Hosono, and S. Okuda, *Appl. Phys. Lett.* **76**, 3319 (2000).
- ²⁵M. Takai, T. Kishimoto, H. Morimoto, Y. K. Park, S. Lipp, C. Lehrer, L. Frey, H. Ryssel, A. Hosono, and S. Kawabuchi, *Microelectron. Eng.* **41/42**, 453 (1998).
- ²⁶P. C. Hoyle, J. R. A. Cleaver, and H. Ahmed, *Appl. Phys. Lett.* **64**, 1448 (1994).
- ²⁷H. W. P. Koops, R. Weiel, D. P. Kern, and T. H. Baum, *J. Vac. Sci. Technol. B* **6**, 477 (1988).
- ²⁸P. C. Hoyle, J. R. A. Cleaver, and H. Ahmed, *J. Vac. Sci. Technol. B* **14**, 662 (1996).
- ²⁹K. T. Kohlmann-von Platen, J. Chiebek, M. Weiss, K. Reimer, H. Oertel, and W. H. Brunger, *J. Vac. Sci. Technol. B* **11**, 2219 (1993).
- ³⁰R. B. Jackson and J. S. Foord, *Appl. Phys. Lett.* **49**, 196 (1986).
- ³¹M. Komuro and H. Hiroshima, *Microelectron. Eng.* **35**, 273 (1997).
- ³²N. A. Kisllov, I. I. Khodos, E. D. Ivanov, and J. Barthel, *Scanning* **18**, 114 (1996).
- ³³K. T. Kohlmann, M. Thiemann, and W. H. Brunger, *Microelectron. Eng.* **13**, 279 (1991).
- ³⁴S. Matsui and K. Mori, *J. Vac. Sci. Technol. B* **4**, 299 (1986).
- ³⁵P. D. Rack, S. Randolph, Y. Deng, J. Fowlkes, Y. Choi, and D. C. Joy, *Appl. Phys. Lett.* **82**, 2326 (2003).
- ³⁶K. R. V. Subramanian, M. S. M. Saifullah, E. Tapley, D.-J. Kang, M. E. Welland, and M. Butler, *Nanotechnology* **15**, 158 (2004).
- ³⁷N. Silvis-Cividjian, C. W. Hagen, P. Kruit, M. A. J. v. d. Stam, and H. B. Groen, *Microelectron. Eng.* **61-62**, 693 (2002).
- ³⁸K. T. Kohlmann-von Platen, J. Chiebek, M. Weiss, K. Reimer, H. Oertel, and W. H. Brunger, *J. Vac. Sci. Technol. B* **11**, 2219 (1993).
- ³⁹H. Hiroshima and M. Komuro, *Nanotechnology* **9**, 108 (1998).
- ⁴⁰H. W. P. Koops, R. Weiel, D. P. Kern, and T. H. Baum, *J. Vac. Sci. Technol. B* **6**, 477 (1988).
- ⁴¹V. Saksena, M. Kushwaha, and S. Khare, *Int. J. Mass Spectrom. Ion Process.* **171**, L1 (1997).

- ⁴²T. Nakano, H. Toyoda, and H. Sugai, *Jpn. J. Appl. Phys., Part 1* **30**, 2912 (1991).
- ⁴³D. A. Alman, D. N. Ruzic, and J. N. Brooks, *Phys. Plasmas* **7**, 1421 (2000).
- ⁴⁴W. Lowell Morgan, C. Winstead, and V. McCoy, *J. Appl. Phys.* **92**, 1663 (2002).
- ⁴⁵R. Basner, M. Schmidt, and H. Deutsch, *Bull. Am. Phys. Soc.* **38**, 2369 (1993).
- ⁴⁶S. Kwitniewski, E. Ptasinska-Denga, and C. Szmytkowski, *Radiat. Phys. Chem.* **68**, 169 (2003).
- ⁴⁷<http://physics.nist.gov/PhysRefData/Ionization/intro.html>
- ⁴⁸S. M. Younger, *J. Quant. Spectrosc. Radiat. Transf.* **26**, 329 (1981).
- ⁴⁹Y.-K. Kim and M. E. Rudd, *Phys. Rev. A* **50**, 3954 (1994).
- ⁵⁰N. Silvis-Cividjian, *Electron Beam Induced Nanometer Scale Deposition*, p. 138.
- ⁵¹H. F. Winters and M. Inokuti, *Phys. Rev. A* **25**, 1420 (1982).
- ⁵²D. C. Joy, *Scanning Microsc.* **5**, 329 (1991).
- ⁵³D. C. Joy and S. Luo, *Scanning* **11**, 176 (1989).
- ⁵⁴S. Luo and D. C. Joy, *Scanning Microsc.* **2**, 1901 (1988).
- ⁵⁵D. C. Joy, *J. Microsc.* **147**, 51 (1987).
- ⁵⁶L. Reimer and C. Tolcamp, *Scanning* **3**, 35 (1980).